

Current-perpendicular-to-plane transport properties of 2D ferromagnetic material $CrTe_2$

Jin Wang(王瑾), Yu Liu(刘宇), Taikun Wang(王太坤), Yongkang Xu(徐永康), Shuanghai Wang(王双海), Kun He(何坤), Yafeng Deng(邓亚峰), Pengfei Yan(闫鹏飞), and Liang He(何亮)

Citation: Chin. Phys. B, 2024, 33 (**9**): 097201. DOI: 10.1088/1674-1056/ad5af1
Journal homepage: http://cpb.iphy.ac.cn; http://iopscience.iop.org/cpb

What follows is a list of articles you may be interested in

Valley-dependent transport in a mescoscopic twisted bilayer graphene device

Wen-Xuan Shi(史文萱), Han-Lin Liu(刘翰林), and Jun Wang(汪军)
Chin. Phys. B, 2024, 33 (**1**): 017205. DOI: 10.1088/1674-1056/acf9e4

Tunable caging of excitation in decorated Lieb-ladder geometry with long-range connectivity

Atanu Nandy
Chin. Phys. B, 2023, 32 (**12**): 127201. DOI: 10.1088/1674-1056/acf5ce

A novel monoclinic phase and electrically tunable magnetism of van der Waals layered magnet $CrTe_2$

Qidi Ren(任启迪), Kang Lai(赖康), Jiahao Chen(陈家浩), Xiaoxiang Yu(余晓翔), and Jiayu Dai(戴佳钰)
Chin. Phys. B, 2023, 32 (**2**): 027201. DOI: 10.1088/1674-1056/ac9b37

Electron tunneling through double-electric barriers on HgTe/CdTe heterostructure interface

Liang-Zhong Lin(林亮中), Yi-Yun Ling(凌艺纭), Dong Zhang(张东), and Zhen-Hua Wu(吴振华)
Chin. Phys. B, 2022, 31 (**11**): 117201. DOI: 10.1088/1674-1056/ac7a0f

Group velocity matters for accurate prediction of phonon-limited carrier mobility

Qiao-Lin Yang(杨巧林), Hui-Xiong Deng(邓惠雄), Su-Huai Wei(魏苏淮), and Jun-Wei Luo(骆军委)
Chin. Phys. B, 2021, 30 (**8**): 087201. DOI: 10.1088/1674-1056/ac0133

Current-perpendicular-to-plane transport properties of 2D ferromagnetic material $CrTe_2$

Jin Wang(王瑾)[1,2], Yu Liu(刘宇)[1,2], Taikun Wang(王太坤)[1,2], Yongkang Xu(徐永康)[1,2], Shuanghai Wang(王双海)[1,2], Kun He(何坤)[1,2] Yafeng Deng(邓亚峰)[1,2], Pengfei Yan(闫鹏飞)[1,2], and Liang He(何亮)[1,2,†]

[1] *School of Electronic Science and Engineering, Nanjing University, Nanjing* 210023, *China*
[2] *State Key Laboratory of Spintronics, Nanjing University, Suzhou* 215163, *China*

(Received 6 May 2024; revised manuscript received 20 June 2024; accepted manuscript online 24 June 2024)

Heterostructures of van der Waals (vdW) ferromagnetic materials have become a focal point in research of low-dimensional spintronic devices. The current direction in spin valves is commonly perpendicular to the plane (CPP). However, the transport properties of the CPP mode remain largely unexplored. In this work, current-in-plane (CIP) mode and CPP mode for $CrTe_2$ thin films are carefully studied. The temperature-dependent longitudinal resistance transitions from metallic (CIP) to semiconductor behavior (CPP), with the electrical resistivity of CPP increased by five orders of magnitude. More importantly, the transport properties of the CPP can be categorized into a single-gap tunneling-through model with the activation energy (E_a) of $\sim$1.34 meV/gap at 300–150 K, the variable range hopping model with a linear negative magnetoresistance at 150–20 K, and weak localization region with a nonlinear magnetic resistance below 20 K. This study explores the vertical transport in $CrTe_2$ materials for the first time, contributing to understand its unique properties and to pave the way for its potential in spin valve devices.

Keywords: 2D vdW, $CrTe_2$, current-perpendicular-to-plane, negative magnetic resistance

PACS: 72.10.–d, 75.50.–y, 81.05.–t, 85.70.–w **DOI:** 10.1088/1674-1056/ad5af1

1. Introduction

Van der Waals (vdW) magnetic materials exhibit layered atomic structures with strong in-plane binding forces and weak interlayer interactions.[1–3] These materials often exhibit novel characteristics due to their unique structures.[4,5] Recently, exploration of new functional devices through stacking of high-quality vdW material heterostructures with different thicknesses has become a prominent avenue.[6–10] In the field of spintronics, a representative device is the spin valve, which constitutes a multilayer heterostructure capable of toggling between two magnetic states.[11,12] Some 2D vdW ferromagnetic materials, such as Fe_3GaTe_2,[13] CrI_3,[14] and Fe_3GeTe_2,[15] have been employed in spin valve magnetoresistance.[16] For example, Fe_3GeTe_2 serves as the ferromagnetic layer with an insulating layer hBN tunnel barrier sandwiched in between, and a typical spin valve magnetoresistance of $\sim$160% has been observed.[17] Additionally, the bilayer CrI_3 structure exhibits a resistance switching ratio of up to 10^2 when a current flow through the spin valve.[18] The elevated magnetoresistance for the devices is attributed to excellent interlayer transport, specifically the current-perpendicular-to-plane (CPP) effect.[19,20] The 2D ferromagnetic materials introduce additional resistance, which affects the performance of spin valve.

$CrTe_2$, as a rising star among the 2D ferromagnetic materials, exhibits excellent thickness-dependent ferromagnetic properties and a tunable Curie temperature (T_C) up to room temperature.[21–23] These characteristics make it suitable for spin valve devices. While extensive research and exploration have been conducted on its characteristics at in-plane current (CIP) mode,[24–26] there is still a blank in understanding the vertical transport properties and mechanisms for $CrTe_2$.

In this work, the resistance characteristics of ultra-thin $CrTe_2$ films with perpendicular magnetic anisotropy (PMA) is analyzed for the CPP mode. The resistivity has increased by five orders of magnitude compared to that of the CIP mode. In the high temperature range (150–300 K), the activation energy (E_a) of approximately 1.34 meV/gap has been found, which is attributed to the tunneling-through mechanism. As the temperature decreases, the variable-range hopping (VRH) mechanism dominates, leading to a linear negative magnetoresistance (NMR). At extremely low temperatures (below 20 K), the observation of weak localization (WL) effects is noted with a nonlinear magnetoresistance (MR). This study marks the first attempt to investigate the CPP transport of $CrTe_2$ thin films, establishing a groundwork for conducting vertical current testing on 2D spin valve devices.

2. Experimental details

On a clean GaAs (111)B substrate, the seven bottom electrodes (3 nm Pt) are fabricated by photolithography and magnetron sputtering. The width of the electrodes is uniformly 10 μm, and the gap between the electrodes is also 10 μm. Subsequently, high-quality $CrTe_2$ films are grown in a molec-

†Corresponding author. E-mail: heliang@nju.edu.cn

© 2024 Chinese Physical Society and IOP Publishing Ltd

ular beam epitaxy (MBE) system (SSI smart-100) under high vacuum conditions (10^{-9} Torr). The growth covered the entire sample, and the XRD characterization of the sample is shown in Fig. S1(b), demonstrating the high quality. Sample thickness depends on RHEED oscillations characterized in Fig. S1(c). Then, the $CrTe_2$ film is patterned into a rectangular shape (20×200 μm) using photolithography and ion beam etching (IBE). Ultimately, three top electrodes (3 nm Pt) are fabricated on the top surface of $CrTe_2$. The schematic diagram of the device is shown in Fig. 1(a), and Fig. 1(b) is a microscopic image of the device.

This structure facilitates conducting CIP and CPP tests on the same sample, enabling a direct comparison and eliminating errors introduced by sample variations. As depicted in the insets of Fig. 1(c), CIP testing entails current between the top and bottom electrodes, which implies that the current primarily flows within the layers. CPP mode involves directing current between the top and bottom electrodes, which implies that the current flows through the vdW gaps. Figure 1(c) illustrates the temperature-dependent resistivities of a 20-layer $CrTe_2$ thin film. The resistivity is obtained according to the formula $\rho = RS/l$. For the CIP mode, as the temperature decreases, the resistivity gradually decreases (to approximately 0.6 mΩ·cm), exhibiting a metallic behavior overall with a kink at 170 K [the black arrow in Fig. 1(c)], representing the T_C, which is consistent with other works.[21–28] In contrast, the CPP mode demonstrates a semiconductor characteristic, and increases by five orders of magnitude from that of CIP, with the resistivity of 1.23×10^5 mΩ·cm at low temperatures.

The temperature dependence remains consistent for other samples of 10 and 40 layers for CPP mode, as illustrated in Fig. 1(d). The resistance at 300 K exhibits a linear dependence on the thicknesses and intercepts the zero as depicted in the inset of Fig. 1(d).

For a deeper comprehension of the charge transport mechanisms of CPP, the modified Arrhenius plots are presented in Figs. 2(b)–2(d). This model can be expressed as[29,30]

$$\rho = \rho_0 T \exp\left(\frac{E_a}{k_B T}\right),$$

where ρ_0 is a pre-exponential factor, E_a is the activation energy, k_B is Boltzmann's constant. In the high-temperature range (150–300 K), the black solid lines are linear fittings for different thicknesses. This verifies the direct tunneling-through model, which involves the entire sample as a barrier, through which charge carriers undergo tunneling-through effects.

Ultimately, the activation energies were obtained to be 14.3 meV, 20.3 meV, and 53.1 meV for 10-, 20-, and 40-layer samples, respectively. As depicted in Fig. 2(e), the activation energy demonstrates a linear dependence on the film thickness. A linear fitting (indicated by the red dotted line) gives the slop of 1.34 meV/gap. It should be noted that for an n-layer sample, there are $(n-1)$ gaps.

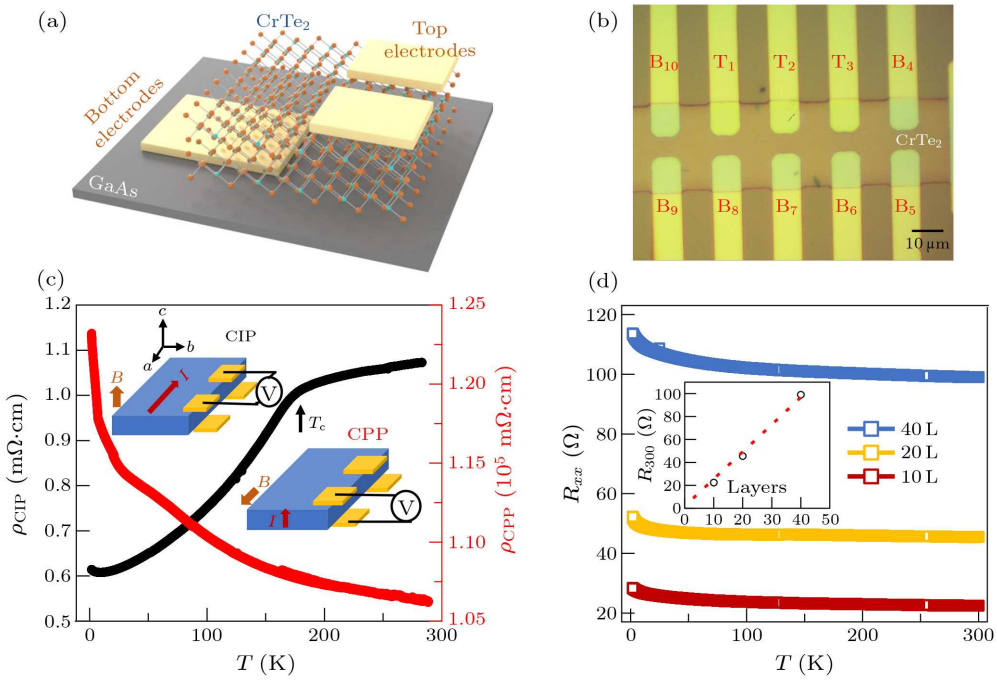


Fig. 1. (a) Schematic representation and (b) optical microscope image of the device. T_1–T_3 represent the three top electrodes, and B_4–B_{10} represent the seven bottom electrodes. Characterization of CIP and CPP transport can be conducted in the same device using the corresponding top and/or bottom electrodes. (c) Temperature-dependent resistivities of CIP and CPP in a 20-layer $CrTe_2$ sample. The resistivity of the CPP mode exhibits a semiconductor behavior, accompanied by a five-order-of-magnitude increase compared to the CIP mode. The insets show the principles of CIP and CPP testing. (d) The CPP measurements of 10-, 20-, and 40-layer samples exhibit the same semiconductor trend, with the resistance linearly dependent on the thickness as shown in the inset.

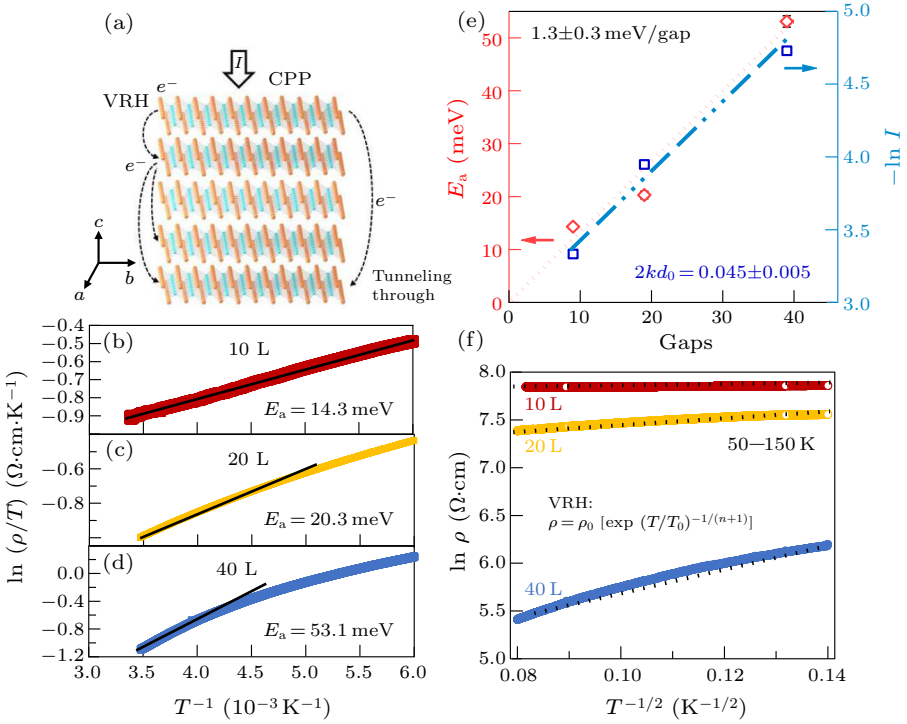


Fig. 2. (a) Illustrations of the tunneling-through and VRH models when the current flows along the *c*-axis. (b)–(d) Modified Arrhenius plots of $\ln(\rho/T)$ vs. T^{-1} for samples with different thicknesses between 160 K and 300 K. Activation energies of 14.3 meV, 20.3 meV, and 53.1 meV can be extracted, respectively. (e) E_a showing a linear correlation with the number of gaps in the red dotted line, resulting in a slop of 1.3 ± 0.3 meV/gap. The logarithm of the tunneling current at a fixed bias voltage of 0.4 mV also exhibits a linear dependence on the gaps, as indicated by the blue dashed line. The fitting results give the average tunneling barrier height of 1.9 meV. (f) Characteristics of $\ln\rho$ vs $T^{-1/2}$. The black dotted lines are linear fittings with the 1D-VRH transition model within the range of 50–150 K.

As mentioned above, the transport process at high temperatures can be treated as a tunneling process. Thus, the electrons tunnel through the multiple vdW's gaps directly. The tunneling current can be expressed as

$$I = C\exp(-2kd),$$

where C is a constant and d is the width of the tunneling gap. Assuming that an interlayer gap distance in a vdW material is d_0, the distance for the n layers sample would be $d = (n-1)d_0$. Here, $k = \frac{2\pi}{h}\sqrt{2m\varphi}$, h is the Planck constant, φ is the tunneling barrier height of the vdW gap, and m is the electron mass.[31]

Then, the magnitude of the $2kd_0$ can be extracted from the linear fitting of $\ln I$ vs n, as shown by the blue dashed line in Fig. 2(e) (detailed calculations can be found in the supplementary note Ⅲ). Adopting the interlayer gap d_0 of 0.11 nm,[32] the tunneling barrier height ϕ is 1.63 ± 0.02 meV. This value closely matches the calculated activation energy of 1.3 ± 0.3 meV mentioned earlier. Thus, the result confirms the direct tunneling-through model at high temperatures for the CPP transport.

Another way of thinking, the thermal energy of the carriers is denoted as $E_R \sim k_B T$. It typically accounts to approximately 25.9 meV at 300 K, which is comparable with the activation energies of 14.3 meV (for 10 layers), 20.3 meV (for 20 layers), and 53.1 meV (for 40 layers). Thus, the direct tunneling-through model is reasonable in the range close to room temperature for the samples.

As the temperature decreases, the thermal energy is insufficient to support the direct tunneling-through model, the electrons randomly move between different layers of the $CrTe_2$, and VRH transition emerges.[33] The resistivity follows the equation provided by this transport model:

$$\rho = \rho_0 \exp\left(\frac{T}{T_0}\right)^{-1/(n+1)},$$

where n is the system's dimension. In the CPP mode of 2D materials, n equals 1, because the electrons only hop along the vertical direction.[34] As shown in Fig. 2(f), the relationship between $\ln\rho$ and $T^{-1/2}$ exhibits a good linearity within the temperature range of 50–150 K for 10-, 20- and 40-layer samples, suggesting the existence of 1D-VRH transport.

Furthermore, the MRs of CIP and CPP modes at various temperatures have been studied, as shown in Figs. 3(a) and 3(b). The applied magnetic field is maintained perpendicular to the current, as shown in the insets of Fig. 1(c). In CIP mode, the magnetic field is oriented parallel to the *c*-axis ($\boldsymbol{B}\|c$), while in CPP testing, it is oriented within the *ab*-plane ($\boldsymbol{B}\|ab$).

In Fig. 3(a), CIP demonstrates a distinctive butterfly-shaped NMR at 2 K (the change in peak position is related to H_C). The distinct magnetic switches observed in both the AHE

(Fig. S5(a)) and MR suggest the presence of a unified magnetic domain for the entire film, eliminating the usual NMR associated with domain wall movements in ferromagnets. In this case, the NMR is likely a result of the linear suppression of magnon populations by external magnetic fields.[35], and the distance between the two peaks represents twice of the coercivity field ($2H_C$). At higher temperatures, the splitting of the peaks decreases as H_C becomes smaller, as shown in Fig. S5(b). This result is consistent with many other reports working on the in-plane transport properties of $CrTe_2$.[36,37]

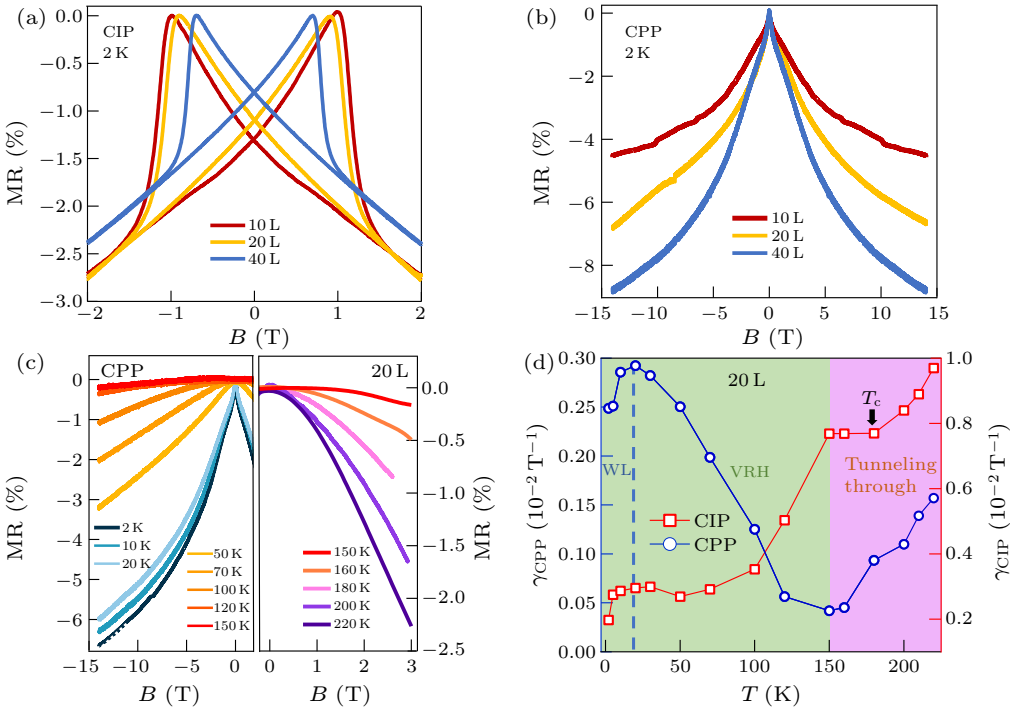


Fig. 3. (a) The CIP mode at 2 K, showing the butterfly-shaped MR, with the magnetic field applied perpendicular to the current ($\boldsymbol{B}\|c$). (b) The CPP mode at 2 K, demonstrating the NMR, with the magnetic field applied perpendicular to the current ($\boldsymbol{B}\|ab$). (c) Temperature-dependent MR for the 20-layer sample from 220 K to 2 K. As the temperature decreases, sharp cusps can be observed at low fields, demonstrating the existence of WL effect. (d) Temperature-dependent MR slopes of CIP and CPP, which are extracted between 12 T and 14 T [white dotted line in (c)]. The γ_{CIP} and γ_{CPP} reveal distinctive trends in the tunneling-through and VRH regions, respectively.

On the other hand, the CPP mode exhibits similar NMR without the splitted peaks, compared to the CIP mode. This is because the out-of-plane ferromagnetism of $CrTe_2$ leaves zero magnetic moment within the plane. Figure 3(c) demonstrates the CPP MR at different temperatures. For all the temperatures, they exhibit unsaturated linear NMR. This can be attributed to the suppression of magnon populations, similar to the CIP mode, and/or the VRH mechanism,[38] which also occurs below 150 K. At 20 K and below, MR exhibits a nonlinear bend, typically associated with the presence of WL effect.[39]

The slopes $\gamma_{CIP} = |\mathrm{dMR_{CIP}}/\mathrm{d}\boldsymbol{B}|$ and $\gamma_{CPP} = |\mathrm{dMR_{CPP}}/\mathrm{d}\boldsymbol{B}|$ at 12–14 T show the non-monotonic temperature dependence in Fig. 3(d). The γ_{CIP} significantly decreases in the high temperature ranges, with a clear step close to its T_C of 170 K. On the other hand, the γ_{CPP} first decreases, then increases and decreases again in the tunneling-through, VRH and WL effect regions, respectively.

Furthermore, the sharp cusps at low fields are typically the fingerprint of WL effect at temperatures below 50 K. The Hikami–Larkin–Nagaoka (HLN) formula is introduced to fit the resistivity in the low magnetic field region:[40,41]

$$\Delta\sigma_{xx} = \frac{\alpha e^2}{2\pi^2\hbar}\left[\psi\left(\frac{l_B^2}{l_\phi^2}+\frac{1}{2}\right)-\ln\left(\frac{l_B^2}{l_\phi^2}\right)\right],$$

where $\Delta\sigma_{xx} = \sigma(H)-\sigma(0)$ represents the change of magnetoconductivity, ψ is the digamma function, e is the electronic charge, and $l_B = \hbar/(4e|B|)$ is the magnetic length. The l_ϕ is the phase coherence length. The α is a pre-factor representing the type of localizations (WL or WAL) and the number of transport channels.

Fitting MR with different thicknesses based on HLN formula (Fig. S7) to obtain the value of α at 2 K. As depicted in Fig. 4(a), α remains close to 0.5, suggesting the presence of one-channel WL phenomena. The temperature-dependent WL for the 20-layer sample has also been fitted, as shown in Fig. 4(b). The α remains around 0.42 with minimal variations as the temperature increases.

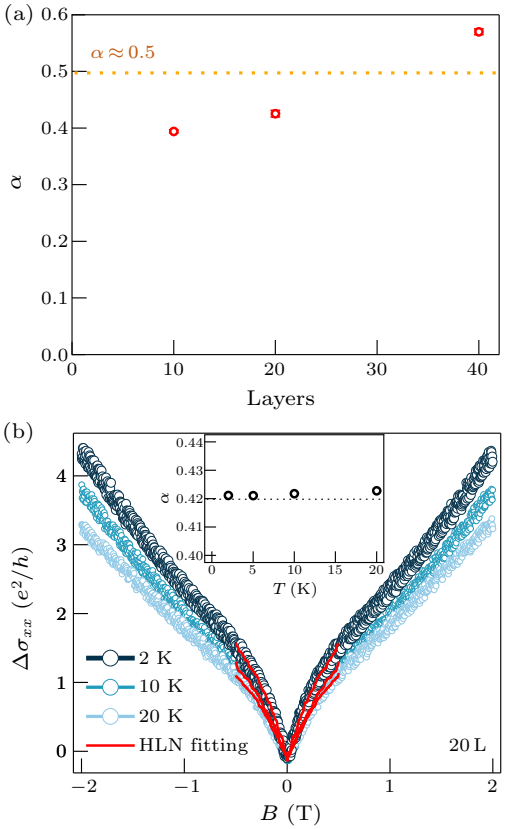


Fig. 4. (a) Relationship between the pre-factor α and thickness, obtained through the HLN fitting at 2 K. Here $\alpha \sim 0.5$ indicates the presence of WL at low temperature. (b) HLN formula fitting performed at different temperatures. The parameter α remains constant.

3. Conclusion and perspectives

In summary, the vertical transport properties of the 2D ferromagnetic material $CrTe_2$ has been studied. A five-order-of-magnitude increase has been found in the resistivity compared with that of CIP mode. From room temperature down to low temperatures, tunneling-through transport is demonstrated with a single interlayer transition energy of 1.34 meV/gap, then the VRH model with linear unsaturated NMR at 20–150 K and WL effect with nonlinear NMR at extremely low temperatures. This study contributes to the understanding of the unique properties of $CrTe_2$ and paves the way for theoretical advancements in applications of spin valve devices.

Acknowledgments

This work was supported by the National Natural Science Foundation of China (Grant Nos. 12241403 and 61974061) and the Natural Science Foundation of Jiangsu Province of China (Grant No. BK20140054).

References

[1] Lin Z, Peng Y, Wu B, Wang C S, Luo Z C and Yang J B 2022 *Chin. Phys. B* **8** 087506
[2] Arai M, Moriya R and Yabuki N 2015 *Appl. Phys. Lett.* **107** 103107
[3] Tian M, Zhu Y and Jalali M 2021 *Front. Nanotechnol.* **3** 732916
[4] Li Q, Yang M M, Gong C, *et al.* 2018 *Nano Lett.* **9** 5974
[5] Wang H D, Lei P H and Mao X Y 2022 *Chin. Phys. Lett.* **39** 047601
[6] Li H, Ruan S C and Zeng Y J 2019 *Adv. Mater.* **27** 1900065
[7] Khajetoorians A A, Wiebe J and Chilian B 2011 *Science* **6033** 1062
[8] Lin Z Z and Chen X 2020 *Adv. Electron. Mater.* **6** 1900968
[9] Zhao B, Ngaloy R, Ghosh S, *et al.* 2023 *Adv. Mater.* **35** 2209113
[10] Yang S X, Zhang T L and Jiang C B 2021 *Adv. Sci.* **8** 2002488
[11] Wu X, Meng H, Kong F, Zhang H Y, Bai Y J and Xu N 2020 *Phys. Rev. B* **101** 125406
[12] Hu C, Yan F, Li Y C and Wang K Y 2021 *Chin. Phys. B* **9** 097505
[13] Jin W, Zhang G, Wu H, Yang L, Zhang W F and Chang H X 2023 *Nanoscale* **15** 5371
[14] Niu Y T, Lu X and Shi Z T 2021 *Chin. Phys. B* **30** 117506
[15] Lin H, Yan F, Hu C, Lv Q S, Zhu W K, Wang Z, Wei Z M, Chang K and Wang K Y 2020 *ACS Appl. Mater. Interfaces* **12** 43921
[16] Wen J, Gaojie Z and Hao W 2023 *Chin. Phys. Lett.* **40** 057301
[17] Wang Z, Sapkota D, Taniguchi T, Watanabe K J, Mandrus D and Morpurgo A F 2018 *Nano Lett.* **18** 4303
[18] Marian D, Soriano D and Cannavó E 2023 *NPJ 2D Mater. Appl.* **1** 42
[19] Roychowdhury A, Dalui T K and Ghose P K 2022 *J. Solid State Chem.* **312** 123106
[20] Klein D R, MacNeill D and Lado J L 2018 *Science* **360** 1218
[21] Sun Y, Yan P and Ning J 2021 *AIP Adv.* **11** 035138
[22] Zhang X, Lu Q, Liu W, *et al.* 2021 *Nat. Commun.* **12** 2492
[23] Zhang H, Chen R, Zhai K, *et al.* 2020 *Phys. Rev. B* **102** 064417
[24] Ren Q D, Lai K, Chen J H, Yu X X and Dai J Y 2023 *Chin Phys. B* **32** 027201
[25] Lasek K, Coelho P M, Zberecki K, Xin Y, Kolekar S K, Li J F and Batzill M 2020 *ACS Nano* **14** 8473
[26] Sun X, Li W, Wang X, *et al.* 2020 *Nano Res.* **13** 3358
[27] Xian J J, Wang C, Nie J H and Li R 2022 *Nat. Commun.* **13** 257
[28] Feng D, Shen Z, Xue Y and Guan Z 2023 *Nanoscale* **15** 1561
[29] Han X, Guo Z, Chen L, Cao C, Sun F, Wang G and Yuan W X 2021 *Mater. Chem. Front.* **5** 8275
[30] Hu L, Cao L, Li L, Duan J M, Liao X Q, Long F C, Zhou J, Xiao Y G, Zeng Y J and Zhou S Q 2021 *Mater. Horiz.* **8** 1286
[31] Bogomolnyd E B and Rouben D C 1999 *Europhys. J. B* **9** 695
[32] Huang C, Liu B, Jiang L, Pan Y F, Fan J Y, Shi D N, Ma C L, Luo Q and Zhu Y 2023 *Phys. Rev. B* **108** 094433
[33] Dau M T, Vergnaud C, Marty A, Rortais F, Beigné C, Boukari H, Bellet-Amalric E, Guigoz V, Renault O, Alvarez C, Okuno H, Pochet P and Jamet M 2017 *Appl. Phys. Lett.* **110** 011909
[34] Sivan U, Entin-Wohlman O and Imry Y 1988 *Phys. Rev. Lett.* **60** 1566
[35] Honglei F, Yong L and Shi Y G 2022 *Chin. Phys. Lett.* **39** 077501
[36] Zhang X Q, Ambhire S C, Lu Q S, *et al.* 2021 *ACS Nano* **15** 15710
[37] Zhu H Y, Gao Y F, Hou Y S, Gui Z G and Huang L 2023 *Phys. Rev. B* **108** 144404
[38] Dau, M T, Vergnaud C, Marty A, *et al.* 2017 *Appl. Phys. Lett.* **110** 4973519
[39] Zhang X, Woods J M, Cha J J and Shi X Y 2020 *Phys. Rev. B* **102** 115161
[40] Sultana R, Gurjar G, Neha P, *et al.* 2018 *J. Supercond. Novel Magn.* **31** 2287
[41] Sharma D, Rani P, Maheshwari P K, Nagpal V, Meena R S, Islam S S, Patnaik S and Awana V P S 2020 *AIP Conf. Proc.* **2220** 110028